ORIGINAL PAPER

Spin distribution of the H-cluster in the H_{ox}–CO state of the [FeFe] hydrogenase from *Desulfovibrio desulfuricans*: HYSCORE and ENDOR study of ^{14}N and ^{13}C nuclear interactions

Alexey Silakov · Brian Wenk · Eduard Reijerse ·
Simon P. J. Albracht · Wolfgang Lubitz

Abstract Hydrogenases are enzymes which catalyze the reversible cleavage of molecular hydrogen into protons and electrons. In [FeFe] hydrogenases the active center is a 6Fe6S cluster, referred to as the "H-cluster." It consists of the redox-active binuclear subcluster ($[2Fe]_H$) coordinated by CN^- and CO ligands and the cubane-like $[4Fe–4S]_H$ subcluster which is connected to the protein via Cys ligands. One of these Cys ligands bridges to the $[2Fe]_H$ subcluster. The CO-inhibited form of [FeFe] hydrogenase isolated from *Desulfovibrio desulfuricans* was studied using advanced EPR methods. In the H_{ox}–CO state the open coordination site at the $[2Fe]_H$ subcluster is blocked by extrinsic CO, giving rise to an EPR-active $S = 1/2$ species. The CO inhibited state was prepared with ^{13}CO and illuminated under white light at 273 K. In this case scrambling of the CO ligands occurs. Three ^{13}C hyperfine couplings of 17.1, 7.4, and 3.8 MHz (isotropic part) were observed and assigned to ^{13}CO at the extrinsic, the bridging, and the terminal CO-ligand positions of the distal iron, respectively. No ^{13}CO exchange of the CO ligand to the proximal iron was observed. The hyperfine interactions detected indicate a rather large distribution of the spin density over the terminal and bridging CO ligands attached to the distal iron. Furthermore, ^{14}N nuclear spin interactions were measured. On the basis of the observed ^{14}N hyperfine couplings, which result from the CN^- ligands of the $[2Fe]_H$ subcluster, it has been concluded that there is very little unpaired spin density on the cyanides of the binuclear subcluster.

A. Silakov · B. Wenk · E. Reijerse (✉) · W. Lubitz (✉)
Max-Planck-Institut für Bioanorganische Chemie,
Stiftstrasse 34-36,
45470 Mülheim a.d. Ruhr,
Germany
e-mail: reijerse@mpi-muelheim.mpg.de

A. Silakov
e-mail: silakov@mpi-muelheim.mpg.de

W. Lubitz
e-mail: lubitz@mpi-muelheim.mpg.de

S. P. J. Albracht
Swammerdam Institute for Life Sciences,
University of Amsterdam,
Nieuwe Achtergracht 166,
1018 WV Amsterdam,
The Netherlands

Abbreviations

|	
CpI	[FeFe] hydrogenase I from *Clostridium pasteurianum*
CW	Continuous wave
DdH	[FeFe] hydrogenase from *Desulfovibrio desulfuricans*
DFT	Density functional theory
ENDOR	Electron–nuclear double resonance
EPR	Electron paramagnetic resonance
ESE	Electron spin echo
ESEEM	Electron spin echo envelope modulation
FID	Free induction decay
FTIR	Fourier transform infrared spectroscopy
HYSCORE	Hyperfine sublevel correlation spectroscopy
Tris	Tris(hydroxymethyl)aminomethane

Introduction

The continuously increasing interest in renewable energy technologies has also stimulated research into hydrogen production using microorganisms [1–3]. Many sulfate-reducing bacteria and monocellular algae make use of H_2 and hydrogenases as part of their energy metabolism.

Three types of hydrogenases can be identified according to the metal content of their active site [1, 4, 5]. For an overview of the field, the reader is referred to the 100th thematic issue of *Chemical Reviews* on hydrogen [6]. [NiFe] hydrogenases have one nickel and one iron atom in their active site [7–9], while [FeFe] hydrogenases accommodate six iron atoms and no other metals [6, 10, 11]. The third class of hydrogenases, the [Fe] hydrogenases, contain a single iron atom in their cofactors [12–14]. This type of enzyme is also called the iron–sulfur-cluster-free hydrogenase [15], or "Hmd" (H_2-forming N^5,N^{10}-methylenetetrahydromethanopterin dehydrogenase).

The structures of two [FeFe] hydrogenases are known so far from X-ray crystallographic studies. One is a periplasmic [FeFe] hydrogenase from *Desulfovibrio desulfuricans* [16] (abbreviated as DdH). The other is a cytoplasmic [FeFe] hydrogenase I from *Clostridium pasteurianum* [17] (abbreviated as CpI). The structures of these hydrogenases exhibit some differences. DdH was found to be a heterodimer containing in total two [4Fe–4S] clusters in addition to the active site. CpI is a monomer with three additional [4Fe–4S] clusters and one [2Fe–2S] cluster. Nevertheless, the structures of the active site (the so-called H-cluster) in these two hydrogenases were found to be very similar [18].

The H-cluster contains six iron atoms arranged in two connected subclusters [16, 18] (Structure 1): a Cys-coordinated $[4Fe–4S]_H$ subcluster, connected to a $[2Fe]_H$ subcluster via a Cys-thiol ligand. Remarkably, each iron in the binuclear subcluster is coordinated by CO and CN^- ligands [19, 20]. The distal iron (relative to the $[4Fe–4S]_H$ subcluster) has an open coordination site, which is believed to be the site for hydrogen binding [6, 21, 22]. Despite extensive investigations of the structure of the H-cluster by various methods, the identity of the central atom in the dithiol bridging ligand has not been resolved yet, so far CH_2, NH, and O were proposed [17, 20, 23, 24]. On the basis of mechanistic considerations, most researchers are inclining to the dithiolmethylamine ligand. However, a recent X-ray crystallographic study of CpI in combination with a theoretical study favored a dithiomethyl ether ligand [24].

Several states of the H-cluster have been observed and characterized by various spectroscopic methods [6, 21]. In contrast to most other [FeFe] hydrogenases, DdH can be isolated aerobically. In this case, it is inactive (H_{inact} state)
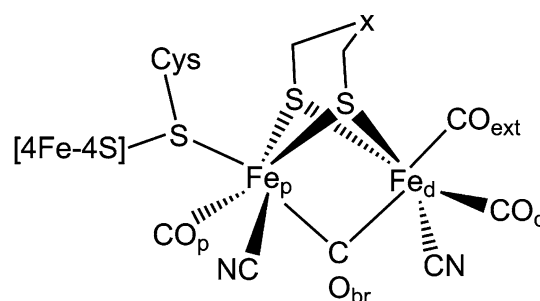
Structure 1

and needs to be activated under reducing conditions. During the activation, it passes through an intermediate state called H_{trans}, which is characterized by a reduction of the $[4Fe–4S]_H^{2+}$ subcluster to a $[4Fe–4S]^+$ state, exhibiting an $S = 1/2$ electron paramagnetic resonance (EPR) signal [25, 26]. The binuclear subcluster remains in an Fe(II)–Fe(II) state [6]. Further lowering of the reduction potential leads to the active oxidized state (H_{ox}), where the $[4Fe–4S]_H$ subcluster is diamagnetic, but the binuclear subcluster is an $S = 1/2$ system [27]. The H_{ox} state of DdH is characterized by a vacant coordination position on the distal iron [6, 28]. In the case of CpI, an X-ray crystallographic study indicated that the open coordination site of the H-cluster is occupied by an oxygen species (H_2O or OH^-) [24]. It is assumed that the irons in the binuclear subcluster are formally in the mixed valence state Fe(I)–Fe(II) and adopt a low-spin configuration, resulting in an $S = 1/2$ EPR signal [26, 27, 29, 30]. According to Mössbauer spectroscopy data, the $[4Fe–4S]_H$ subcluster remains in the formal 2+ ($S = 0$ ground state) state in all active states of the H-cluster investigated [29].

The fully reduced state of the H-cluster (H_{red}) is EPR-silent. It is characterized by the Fe(I)–Fe(I) valence state of the binuclear subcluster [6, 30, 31]. According to Fourier transform (FT) IR and crystallographic studies, the bond between the bridging CO ligand and the proximal iron is broken upon reduction of H_{ox} and so this CO ligand is then bound in a terminal position to the distal iron [19, 20, 31].

Inhibition of the active enzyme by CO has been investigated by various methods, including X-ray crystallography. It has been shown that extrinsic CO binds to the distal iron, leading to inactivation of the [FeFe] hydrogenase (the so-called H_{ox}–CO state) [31–34]. The CO-inhibited state shows an $S = 1/2$ EPR signal [35]. Earlier investigations of this state showed that it is an Fe(I)–Fe(II) mixed valance state, similar to the H_{ox} state [31, 33, 34]. Our recent ^{57}Fe study has shown that in this state the spin density is mostly located around the proximal iron. On the basis of these results, together with recent FTIR studies, a formal $Fe_p(I)–Fe_d(II)$ state has been suggested [30, 31, 34].

Upon illumination of a liquid solution of enzyme in the H_{ox}–CO state at temperatures between 275 and 278 K, the

extrinsic CO ligand can be reversibly dissociated [19, 31]. In the frozen state and at temperatures below 60 K this leads to the generation of the H_{ox} state. In addition, another photodissociated state is formed and is characterized, most probably, by the loss of the bridging CO ligand. It has been shown that by increasing the temperature above 150 K, one can fully restore the H_{ox}–CO state [31, 36].

Clostridium pasteurianum was believed to contain two [FeFe] hydrogenases. Both hydrogenases have been investigated in the H_{ox}–^{13}CO state by continuous-wave (CW) EPR and CW electron–nuclear double resonance (ENDOR) [37, 38] at X-band frequencies. CpI revealed a single quite isotropic ^{13}C hyperfine coupling of 20–22 MHz[1] [37]. [FeFe] hydrogenase II from *C. pasteurianum* showed a rather different ^{13}C hyperfine coupling, with principal values of $A_1 = 34.0$ MHz, $A_2 = 36.0$ MHz, and $A_3 = 29.0$ MHz [38]. Since it is not clear whether this species represents a genuine second hydrogenase in the bacterium, or merely a breakdown product of CpI [6], we will not discuss these data in detail. DdH has also been studied in the ^{13}CO-inhibited form. The CW EPR spectrum of the H_{ox}–^{13}CO state has been compared with that of nonenriched hydrogenase. Simulation of the line broadening indicated a single isotropic ^{13}C hyperfine coupling of about 17 MHz [34]. The same authors investigated the effects of illumination at 275 K of the H_{ox}–^{13}CO state [31, 34]. It was found that upon prolonged illumination the IR bands assigned to the bridging CO and to the terminal CO of the distal iron shifted to longer wavelengths; therefore, it was proposed, that these two ligands exchanged with the extrinsic ^{13}CO (so-called scrambling effect) [31, 34]. However, comparison of the EPR spectra before and after illumination did not reveal any additional broadening of the lines; therefore, it was concluded that only the ^{13}C of the extrinsic CO ligand has a large hyperfine coupling, while the hyperfine coupling constants of ^{13}C of the CO_d and the CO_{br} ligands are too small to be observed at X-band EPR.

Structurally, the H-cluster is believed to be well preserved in all [FeFe] hydrogenases. However, variations in the spectroscopic properties of the H-clusters from different organisms (including the newly studied [FeFe] hydrogenases from green algae) may indicate distinct structural differences [6, 30, 40]. It is very important to determine the electronic structure of the H-cluster in great detail to understand what may cause these variations. Our recent study of the ^{57}Fe hyperfine couplings in DdH showed delocalization of the unpaired spin over both irons in the binuclear subcluster, depending on the state of the H-cluster [30]. More details about the electronic structure

can be obtained from investigations of magnetic ligand nuclei in the binuclear subcluster. Here we present a pulse EPR investigation of the ^{14}N and ^{13}C nuclear spin interactions of the CO and CN$^-$ ligands for the H_{ox}–CO state of DdH. Also the effects of illumination of the H-cluster detected by this technique will be discussed.

It is shown that ^{13}C hyperfine couplings can be extracted from hyperfine sublevel correlation spectroscopy (HYSCORE) and ENDOR spectra with high precision, allowing the assignment of the signals obtained to different CO ligands. The observed ^{13}C signals were also used to understand the scrambling of the CO ligands under light. In addition, information about ^{14}N interactions has been obtained, which is important to understand the distribution of the unpaired spin density over the CN$^-$ ligands of the irons in the binuclear subcluster.

Materials and methods

EPR setup

X-band measurements were performed using a Bruker Elexsys E-580 X-band spectrometer equipped with a SuperX-FT microwave bridge and an Oxford Instruments CF935 helium-flow cryostat. Pulse EPR, ENDOR, and HYSCORE spectra were obtained using a Bruker EN 4118X-MD4 dielectric ENDOR resonator with an Applied Systems Engineering 1-kW traveling wave tube amplifier (model 117x). CW EPR measurements were performed with the same spectrometer using a Bruker ER 4118X-MD5 dielectric resonator without ENDOR coils.

All Q-band HYSCORE and pulse ENDOR measurements were performed using a Bruker Elexsys E 580 Q-band spectrometer equipped with a SuperQ-FT microwave bridge and an Oxford Instruments CF935 flow cryostat at temperatures ranging from 10 to 20 K. For these measurements we used a slightly overcoupled cylindrical TE_{011} homebuilt resonator with a construction similar to that described by Sienkiewicz et al. [30, 41].

For pulse ENDOR experiments with the random-acquisition procedure we used a homebuilt data acquisition system, based on SpecMan software on a personal computer [42]. The Bruker spectrometer was used to generate microwave pulses and to trigger the SpecMan system, which in turn controls the generation of radiofrequency pulses and records the signal coming from the Bruker spectrometer. In these experiments the radiofrequency pulses were generated by an Agilent E4420B radiofrequency generator and amplified by a high-power AR 2500L radiofrequency amplifier from Amplifier Research™, running in CW mode (2,500-W output). To suppress the "harmonics" of the ^{1}H ENDOR signals (around 51 MHz at

---

[1] Recently the study was repeated using Q-band CW ENDOR. The measurements resulted in an isotropic ^{13}C hyperfine coupling of 20 MHz [39].

1.2 T), a Trilithic^{TM} H4LE35-3-AA-R high-power low-pass filter (cut-off frequency about 35 MHz) was used.

EPR methods

Q-band EPR spectra were obtained using free induction decay detected EPR with a 1-μs microwave pulse. This length of the microwave pulse was found to be sufficient to suppress field-dependent distortions in the absorption-like spectrum due to the presence of magnetic nuclei. To facilitate the comparison with CW X-band spectra, free induction decay detected spectra were differentiated using the so-called pseudomodulation procedure described by Hyde et al. [43].

HYSCORE [44] was used to extract most of the parameters of ^{13}C and ^{14}N nuclear interactions. The pulse sequence for this method was

$$[\pi/2] - \tau - [\pi/2] - t_1 - [\pi] - t_2 - [\pi/2] - \tau - (\text{ESE}).$$

This is a 2D method, in which the intensity of the stimulated electron spin echo (ESE) is detected as a function of delays t_1 and t_2. The 2D modulation pattern obtained was processed using third-order background polynomial subtraction and Hamming apodization followed by zero-filling and 2D fast Fourier transformation.

X-band HYSCORE spectra were obtained using an 8-ns microwave pulse for the "π/2" pulses and a 16-ns microwave pulse for the "π" pulse. The delay between the first two pulses (τ) was adjusted according to an ESE envelope modulation (ESEEM) experiment in which a three pulse ESEEM spectrum is recorded as a function of τ [45, 46]. To suppress the effects of unwanted echoes, a four-step phase cycling of the microwave pulses was used [47]. An additional set of experiments was performed using pulse ENDOR at Q-band frequency utilizing the Davies ENDOR sequence [48]:

$$[\pi] - t_{d1} - [RF] - t_{d2} - [\pi/2] - \tau - [\pi] - \tau - (\text{ESE}).$$

The excitation of nuclear spin transitions is detectable through a reduction of the ESE intensity. The length of the radiofrequency (RF) pulse was adjusted to maximize the ENDOR effect of the high-frequency feature in the ^{13}C ENDOR spectrum. The delay before the radiofrequency pulse (t_{d1}) was set to 1 μs. It has been found that the delay between the radiofrequency pulse and the detection sequence (t_{d2}) needs to be longer then 3 μs to avoid distortions in the ENDOR spectra.

Simulations

Simulation of the spectra were based on the spin Hamiltonian approach using

$$\hat{\mathcal{H}}_0 = \beta \vec{B} \cdot \mathbf{g} \cdot \hat{S} + \sum \mu_n g_n{}^i \vec{B} \cdot \hat{I}_i \\ + \sum \hat{S} \cdot \mathbf{A}_i \cdot \hat{I}_i + \sum \hat{I} \cdot \mathbf{P}_i \cdot \hat{I}_i, \tag{1}$$

where β is the Bohr magneton, $\vec{B}$ the magnetic field vector, $\hat{S}$ the electron spin operator, $\mathbf{g}$ the g tensor, μ_n the nuclear magneton, g_n the nuclear g value, $\mathbf{A}_i$ the hyperfine tensor, $\hat{I}_i$ the nuclear spin operator, $\mathbf{P}_i$ the nuclear quadrupole tensor, and the sums run over all nuclei (i), interacting with the unpaired electron spin. The first and the second terms represent the electron and the nuclear Zeeman effects, the third term is the hyperfine interaction of the unpaired electron and the nuclear spins, and the last term represents the quadrupole interaction of the nuclear spins for nuclei with $I > 1/2$.

The quadrupole tensor $\mathbf{P}$ is traceless. The representation in its principal axis system (in frequency units) can be written in the following way:

$$[P_x, P_y, P_z] = \frac{e^2 qQ}{4I(2I-1)h}[-(1-\eta), -(1+\eta), 2]. \tag{2}$$

Here we will use two variables to characterize the quadrupole coupling:

$$K = \frac{e^2 qQ}{4I(2I-1)h}$$

and

$$\eta = \frac{P_x - P_y}{P_z}.$$

Orientations of the hyperfine and quadrupole tensors are presented with respect to the g tensor using Euler angles. In the calculations we used the "y" convention for the Euler angles, in which the first angle (α) "rotates" along the z-axis, the second angle (β) along the y'-axis, and the third (γ) along the z''-axis [45].

ENDOR spectra were simulated using the "salt" routine of the EasySpin package [49] for MATLAB^{TM} [50]. Frequency-domain calculations of HYSCORE spectra were facilitated using home-written routines for MATLAB^{TM} [50] utilizing a general expression for the nuclear modulation signal for the case of ideal microwave pulses, presented by Shane et al. [51]. The case of several interacting nuclei was treated according to the product rule for HYSCORE [52].

Growth of D. desulfuricans ATCC 7757

Desulfovibrio desulfuricans cultures were grown for three days in a 10-L glass fermenter with an automatic pH control unit, which kept the pH within a range of 6.5–8. The medium contained 2.0 g $MgSO_4 \cdot 7H_2O$, 5.0 g sodium citrate·2H$_2$O, 1.0 g $CaSO_4 \cdot 2H_2O$, 1.0 g NH_4Cl, 0.5 g K_2HPO_4, 7.0 g sodium lactate, and 1.0 g yeast extract in

1 L H_2O, pH 7.5. Lactate, K_2HPO_4, and yeast extract were autoclaved separately to avoid an undesired precipitation of the medium. These three media were afterwards mixed aseptically and 5 mL of a sterile filtered solution of 20% $Fe(NH_4)_2(SO_4)_2 \cdot 6H_2O$ was added. During the growth, the culture was fed with 200 mL 50% lactic acid per day, divided into small portions.

The growth medium was kept anaerobic by constant bubbling with nitrogen. The dense culture was then harvested aerobically by centrifugation and the wet cell pellet (46 g) was stored at 193 K.

Isolation of DdH

The isolation followed the purification protocol of Hatchikian [53], originally established by van der Westen [54]. The wet cell pellet (46 g) of a harvested *D. desulfuricans* was incubated for 30 min at room temperature in a buffer with 50 mM Na_2-EDTA and 50 mM tris (hydroxymethyl)aminomethane (Tris)/HCl (adjusted to pH 9 with HCl) under gentle stirring to obtain the periplasmic fraction, which contains the [FeFe] hydrogenase. This fraction was then separated from the cells by centrifugation at 35,000*g* for 30 min. The periplasm was precipitated with ammonium sulfate in 50 and 80% saturation steps at room temperature and centrifuged as mentioned above. The second precipitate contained the hydrogenase.

The precipitate was dialyzed overnight against 10 mM Tris/HCl buffer, concentrated, and then loaded on a DEAE 52 ion-exchange column. The resulting chromatogram showed three major peaks. From these peaks, selected fractions were tested for hydrogenase activity via a qualitative test with methyl viologen: 100-μL sample and 2 mL 25 mM Tris/HCl buffer comprising an excess of methyl viologen (approximately 0.8 M) were sealed in a glass vial and the glass vial was connected to a hydrogen-gas line. After 2–3 min of flushing with hydrogen, hydrogenase-containing fractions turn blue as the electrons from the oxidation of molecular hydrogen convert methyl viologen into its blue reduced radical form. Active fractions were pooled and further purified by a Sephacryl S 200 gel filtration column. A Biogel K-phosphate column finally separated the pooled concentrated fractions. The elution profile showed a single peak of active fractions, which were desalted by a PD-10 column and concentrated to a volume of 50 μL by Millipore Centriprep concentrators. The purity of the sample was monitored with sodium dodecyl sulfate polyacrylamide gel electrophoresis and showed two distinct bands representing the small and the large subunit, respectively (not shown). The concentration of the protein was calculated with the aid of UV/vis spectra of the sample. The purified

enzyme (0.6 mg) was stored in a liquid nitrogen tank. The procedure was repeated twice and yielded samples of similar concentrations.

Treatment of the samples with gas

To activate the aerobically isolated [FeFe] hydrogenase, we followed the procedure described by Hagen et al. [55]. The sample in the sealed glass vial was flushed with hydrogen gas after evacuation of the vial. The procedure was repeated several times within 15 min. To obtain the H_{ox} state, hydrogen was replaced by argon and the procedure was repeated several times for another 15 min. The CO-inhibited state (H_{ox}–CO) was obtained by flushing the enzyme in the H_{ox} state with CO gas for 15 min. To prepare the H_{ox}–^{13}CO state, ^{13}C-enriched CO gas (99% enriched in ^{13}C and containing less than 10% ^{18}O) from Cambridge Isotope Laboratories was used. After a gas treatment, the sample was transferred to the EPR tubes in an anaerobic glove box (Coy Laboratory Products) under a nitrogen atmosphere with an admixture of 2% hydrogen. Subsequently, the EPR samples were frozen in liquid nitrogen.

Results

Figure 1 shows the X- and Q-band CW EPR spectra of H_{ox}–CO from DdH. The spectrum is characteristic for all [FeFe] hydrogenases, from both bacterial and algal sources [6]. The slight rhombicity of the *g* tensor has already been discussed by Silakov et al. [30] and Albracht et al. [34] on the basis of X-band EPR but it is better resolved at Q-band.

The spectra can be simulated using the following principal *g* values:

$$g_1 = 2.065, \quad g_2 = 2.007, \quad g_3 = 2.001.$$

Remarkably, the slight rhombic distortion observed for the *D. desulfuricans* spectra was not present in the EPR spectra of other [FeFe] hydrogenases from *C. pasteurianum* [37, 38] and from *C. reinhardtii*, *C. submarinum*, and *C. moewusii* [40]. The unpaired spin density distribution is very sensitive to the geometry of the molecule. Thus, differences in the observed *g* values are most probably related to slight geometrical variations, caused by the protein surroundings in the different [FeFe] hydrogenases. Accurate measurements of the ^{13}C and ^{14}N nuclear spin couplings in the H-cluster of the CO ligands and the CN^- ligands, respectively, yield information on the electronic structure and its variation among the different [FeFe] hydrogenases. The findings of such experiments, performed on DdH, are presented in the following sections.
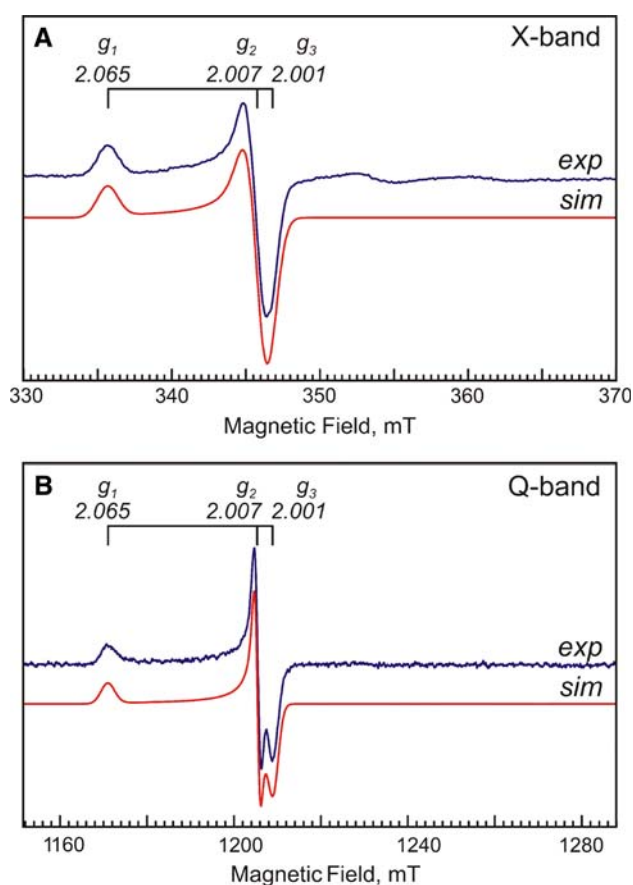
Fig. 1 X- and Q-band electron paramagnetic resonance (EPR) spectra of the H_{ox}–CO state of the H-cluster measured at 40 K (*blue*) and simulations (*red*) using the *g* values shown for each experimental spectrum. Spectra are displayed on the same *g* value scale to facilitate a direct comparison. The experimental conditions were as follows: **a** continuous-wave (CW) EPR, P_{mw} 20 μW (40-dB attenuation), ν_{mw} 9.7134 GHz, time constant 40.96 ms, conversion time 81.92 ms, modulation amplitude 0.5 mT, modulation frequency 100 kHz; **b** free induction decay detected EPR, microwave pulse length 1 μs, shot repetition time 500 μs, ν_{mw} 33.8485 GHz. To facilitate direct comparison with the X-band CW EPR spectrum (**a**), the first derivative of the spectrum is presented

^{14}N interactions of the CN$^-$ ligands

The ^{14}N hyperfine couplings provide important information about the distribution of unpaired spin density over the CN$^-$ ligands in the binuclear subcluster (Structure 1). Since ^{14}N has a nuclear spin of $I = 1$, additional information can be obtained from the quadrupole interaction, which probes the electric field gradient and thus the intimate surroundings of the ^{14}N nucleus. Nuclear quadrupole couplings are characteristic for a nucleus in a specific bonding situation.

The investigation was performed at X-band frequency using HYSCORE. Several HYSCORE spectra were measured at various positions of the magnetic field. It should be noted that the rhombic distortion of the high-field

component of the X-band EPR spectrum is about 0.8 mT, while the excitation bandwidth of the 16-ns microwave pulse is about 3.0 mT. Thus, the HYSCORE spectrum measured at g_2 is considered to contain all orientations related to both g_2 and g_3. The resulting X-band HYSCORE spectra measured for the H-cluster in the H_{ox}–CO state are shown in Fig. 2.

The HYSCORE spectra revealed two separate sets of crosspeaks in the (++) quadrant, while no signals were observed in the (+−) quadrant (not shown). One set of peaks around 15 MHz is centered at the Larmor frequency of the ^{1}H nucleus [$\nu_n(^1H) = 14.81$ MHz at 347.9 mT]. It is assumed that these signals originate from the nonexchangeable β-protons of the Cys ligands of the [4Fe–4S]$_H$ subcluster [37]. As observed for various [4Fe–4S]-containing systems [56, 57], these ^{1}H nuclear spins exhibit relatively large dipolar hyperfine couplings. Since all ^{1}H signals are overlapping in the "powder" spectra,[2] the analysis cannot yield all hyperfine coupling parameters. We expect that EPR and ENDOR studies of single crystals of [FeFe] hydrogenase would be ideal to determine these interactions.

Apart from the ^{1}H signals, the low-frequency part of the HYSCORE spectra (3–4 MHz) shows another set of crosspeaks. The field dependence of these crosspeaks can be fitted as ^{14}N nuclear spin interactions. According to our experience, crosspeaks of $\Delta M_I = 2$ transitions can be more pronounced in HYSCORE spectra than $\Delta M_I = 1$ transitions, depending on the magnitude of the quadrupole and the hyperfine interactions. Therefore, the peaks around 3.5 MHz are assigned to double quantum transitions of a ^{14}N nuclear spin. The shallow peak at about 1.7 MHz in Fig. 2c might represent a single quantum transition. The low-frequency region of the HYSCORE spectra, taken at the g_2 and g_1 positions, is shown in Fig. 2b and c.

The simulation of these spectra (Fig. 2d, e) yields the hyperfine and quadrupole parameters summarized in Table 1. Remarkably, the weak crosspeaks at 1.7 MHz could also be reproduced (Fig. 2e).

It was anticipated that the nitrogens from two CN$^-$ ligands would contribute to the HYSCORE spectrum; however, only one interacting ^{14}N nucleus was sufficient to simulate the experimental data (Fig. 2d, e). This indicates a localization of the unpaired spin density on one of the iron atoms. Thus, strongly different hyperfine couplings for the two nitrogen nuclei of the CN$^-$ ligands are expected. If the observed ^{14}N signals are from the nucleus with the largest hyperfine coupling, then the other ^{14}N hyperfine coupling might be too small to be observed. On the other hand, since these crosspeaks are not well resolved, a contribution from

---

2 It is expected to find signals from at least eight ^{1}H nuclei, two β-protons on each of the coordinating Cys ligands.
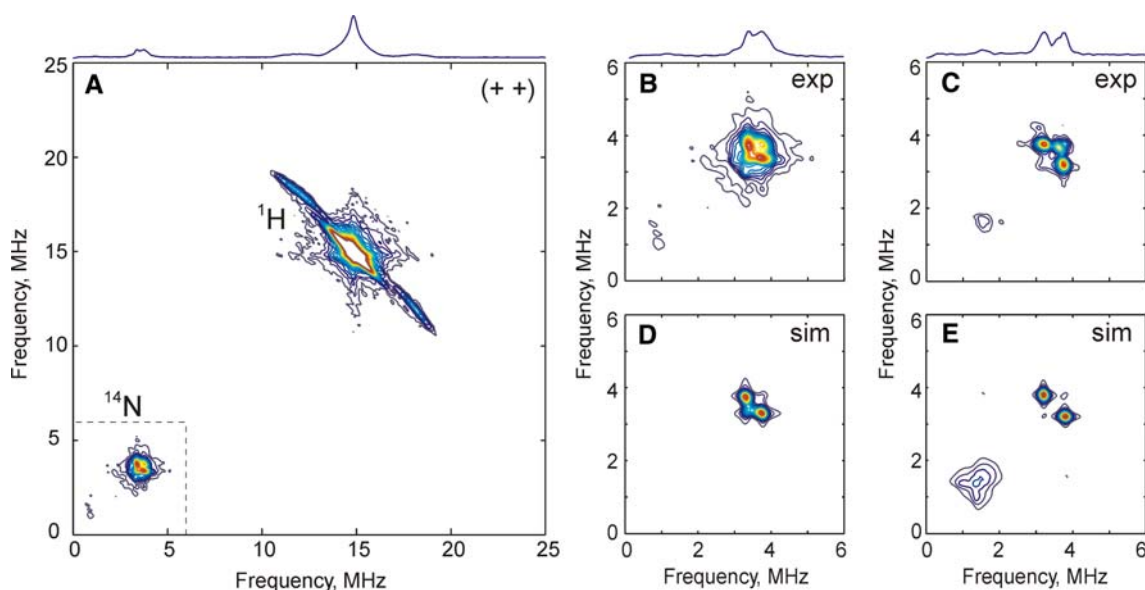
Fig. 2 X-band hyperfine sublevel correlation spectroscopy (HY-SCORE) spectra of the nonlabeled H_{ox}–CO state of the H-cluster in *Desulfovibrio desulfuricans* measured at 20 K: **a** complete spectrum, measured at 347.9 mT (g_2) [the (+−) quadrant shows no signals and thus is not shown]; **b** low-frequency part (^{14}N signals) of **a**; **c** low-frequency part of the HYSCORE spectrum taken at 338.1 mT (close to g_1); **d** and **e** simulations of the ^{14}N signals in the spectra shown in **b** and **c**, respectively, involving only one ^{14}N nucleus and using the parameters given in Table 1. The experimental conditions were as follows: ν_{mw} 9.7833 GHz; τ 120 ns; t_1 and t_2 step 16 ns; shot repetition time 2 ms

Table 1 Parameters of the hyperfine and quadrupole coupling of the ^{14}N nucleus, from the analysis of hyperfine sublevel correlation spectroscopy spectra (HYSCORE)

Hyperfine coupling						Quadrupole coupling				
$A_{x'}$ (MHz)	$A_{y'}$ (MHz)	$A_{z'}$ (MHz)	α (°)	β (°)	γ (°)	K (MHz)	η (MHz)	α (°)	β (°)	γ (°)
0.40 (10)	−0.20 (10)	0.56 (5)	0 (20)	−10 (20)	0 (20)	0.76 (1)	0.64 (5)	0 (20)	30 (10)	0 (20)

The sign of the hyperfine couplings has not been determined. Numbers in *parentheses* are uncertainties in units of the least significant digit

two ^{14}N nuclear spins cannot be completely excluded. Remarkably, the magnitude of the quadrupole coupling is somewhat smaller than is usually found for CN⁻ ligands (0.9–1.5 MHz) [58, 59]. According to the analysis of the X-ray crystallographic structure, a hydrogen bond from the closest amino acid to the nitrogen of the CN⁻ ligand may be formed [23, 24]. In the DdH X-ray crystallographic structure (Protein Data Bank ID 1HFE) they are Ile204, Lys237, and Ala109. Hydrogen bonding to CN⁻ is expected to decrease the magnitude of the quadrupole coupling.

Here one should mention another possible source of the observed ^{14}N signals. Reanalysis of the X-ray crystallographic structure together with some theoretical studies have proposed a –CH₂–NH–CH₂– moiety for the bridging dithiol ligand in the binuclear subcluster (Structure 1) [20, 60]. Therefore, the observed ^{14}N signals could also originate from this ligand, though it seems unlikely, owing to its remote position with respect to the iron atoms. Moreover, the quadrupole coupling of this ^{14}N nucleus (secondary amine) is expected to be larger (about 1.2 MHz) [58] than was observed experimentally. Since the observed hyperfine interaction points to a weakly coupled ^{14}N nucleus, we conclude that there is only very little unpaired spin density on the CN⁻ ligands of the binuclear subcluster.

^{13}C interactions of the CO ligands

More information about the distribution of the unpaired spin density can be obtained from the investigation of the ^{13}C hyperfine couplings of the CO ligands. The ^{13}CO-inhibited state (H_{ox}–^{13}CO) can be easily obtained from the oxidized active state of the H-cluster by flushing it with ^{13}C-enriched CO gas for 15 min. The H_{ox}–^{13}CO sample reveals a moderately broadened X-band CW EPR signal in comparison with the nonenriched sample (Fig. 3). The broadening of the EPR spectrum due to labeling with the ^{13}C isotope can be simulated using one isotropic ^{13}C hyperfine coupling of 0.60 mT (16.8 MHz), as described before [34].
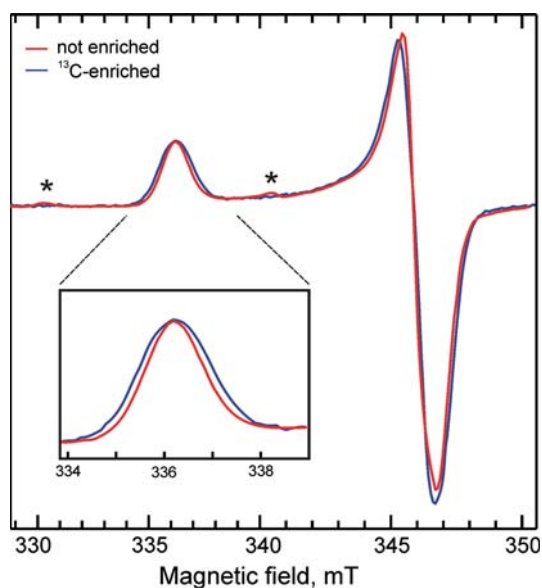
Fig. 3 Comparison of X-band CW EPR spectra of the H_{ox}–CO (*red*) and the H_{ox}–^{13}CO (*blue*) states. The experimental conditions are the same as for the X-band CW EPR spectrum presented in Fig. 1a. *Asterisks* indicate a minor contribution of the H_{ox} state due to incomplete inhibition of the H-cluster by CO

However, since the hyperfine splitting is not resolved in the EPR, more precise methods need to be applied to obtain the parameters of the hyperfine tensor with high accuracy. Therefore, we performed pulse EPR and ENDOR spectroscopy on H_{ox}–^{13}CO.

HYSCORE spectra at X-band were measured at several positions of the external magnetic field. Apart from the ^{14}N and ^{1}H signals described above, an additional pair of crosspeaks was identified in these spectra. The spectrum measured at the position of highest EPR intensity (g_2) is shown in Fig. 4.

The pair of crosspeaks in the (+−) quadrant can be exclusively assigned to one ^{13}C nucleus because it is not present in the spectra of the nonenriched sample.
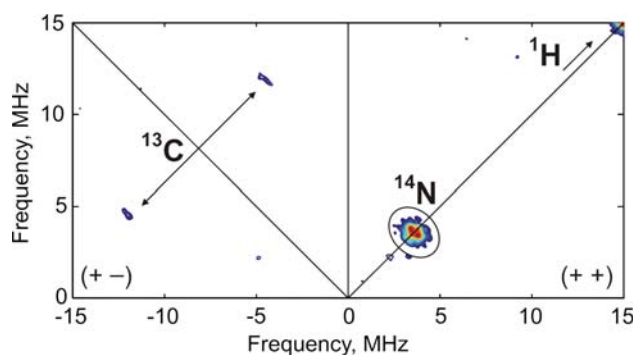

Fig. 4 X-band HYSCORE spectrum [(+−; *left*) and (++; *right*) quadrants] of the H_{ox}–^{13}CO state. The experimental conditions were as follows: B_0 346.8 mT (g_2); v_{mw} 9.7607 GHz; τ 120 ns; t_1 and t_2 step 16 ns; shot repetition time 2 ms

Moreover, the crosspeaks are separated by twice the Larmor frequency of a ^{13}C nucleus ($v_n(^{13}C) = 3.75$ MHz at 350 mT). The orientation-selective experiments reveal that this hyperfine interaction is very anisotropic. The field-dependent hyperfine coupling constant increases with decreasing magnetic field. Unfortunately, a complete analysis is not possible using this method since at the lower magnetic field (around g_1) these signals are not observable in the HYSCORE spectra (data not shown here). It is well known that signals from nuclei with hyperfine couplings close to exact cancellation ($A \approx 2v_n$) are most prominent in ESEEM spectra, while signals from strongly coupled nuclei vanish with increasing hyperfine coupling constant [61]. Apparently, at this field position the NMR frequencies of the ^{13}C signals are too large to be detected using this method; therefore, additional Q-band ENDOR measurements were performed to extract all the parameters of this ^{13}C hyperfine coupling. At this microwave frequency (about 34 GHz) the ^{13}C signals are well separated from the ^{1}H signals and only partially overlap with the ^{14}N peaks, which are, in fact, hardly detectable. Figure 5 shows Davies ENDOR spectra together with their simulation (see hyperfine coupling A_{1C} from Table 2).
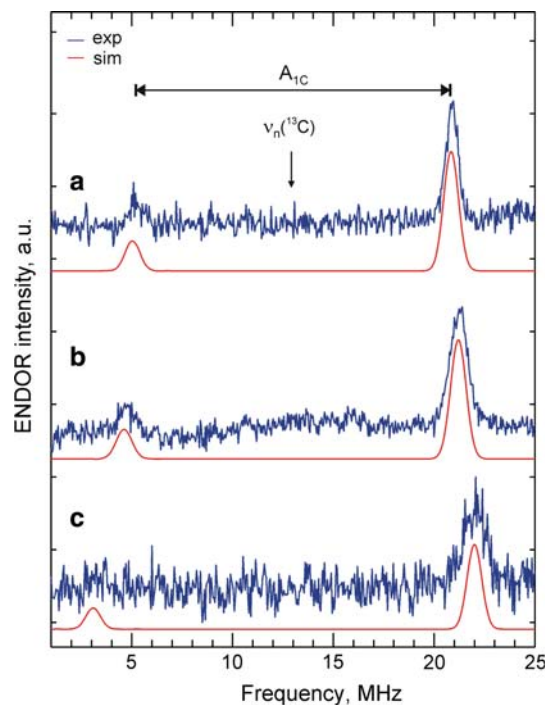

Fig. 5 Q-band Davies electron–nuclear double resonance (*ENDOR*) spectra of the H_{ox}–^{13}CO state, measured at several positions of the magnetic field (*blue*) and simulations using values of the A_{1C} hyperfine coupling from Table 2 (*red*). The experimental conditions were as follows: temperature 15 K; v_{mw} 33.8505 GHz; shot repetition time 2 ms; length of the radiofrequency pulse 25 µs; B_0 **a** 1,207.8 mT (g_3), **b** 1,204.7 mT (g_2), **c** 1,170.7 mT (g_1)

Table 2 Principal values of the ^{13}C hyperfine tensor and assignment of different couplings to the CO ligands of the binuclear subcluster

	$A_{x'}$ (MHz)	$A_{y'}$ (MHz)	$A_{z'}$ (MHz)	A_{iso} (MHz)	α (°)	β (°)	γ (°)	Assignment
A_{1C}	15.6 (2)	16.6 (2)	19.2 (2)	17.1	0 (10)	0 (10)	0 (10)	CO_{ext}
A_{2C}	8.5 (3)	9.8 (3)	3.9 (2)	7.4	50 (20)	20 (10)	50 (20)	CO_{br}
A_{3C}	3.2 (2)	3.7 (2)	4.4 (1)	3.8	0 (20)	40 (10)	0 (10)	CO_d

The signs of the hyperfine couplings have not been determined. Numbers in *parentheses* are uncertainties in units of the least significant digit

From the X-ray crystal structure of CpI it is known that upon reaction of the H-cluster with CO gas, the extrinsic CO binds to the open coordination site of the distal iron [32] (Structure 1). Since the FTIR spectra of DdH and CpI are rather similar for the CO-treated samples (H_{ox}–CO state), it can be assumed that in the case of *D. desulfuricans* the binding site for the exogenous CO is the distal iron as well. Hence, the extracted ^{13}C hyperfine tensor was assigned to the extrinsic CO ligand of the distal iron (CO_{ext}). Earlier ENDOR studies of the H_{ox}–^{13}CO state of the active site of CpI revealed a single ^{13}C hyperfine coupling of about 21 MHz [37]. The extracted ^{13}C hyperfine tensor was found to be rather isotropic (the dipolar contribution is less than 2 MHz). This differs from the A_{1C} coupling, which has a larger dipolar contribution and is somewhat smaller. This is in agreement with our previous study, in which the ^{57}Fe hyperfine couplings of the H_{ox} and H_{ox}–CO states of DdH were also found to be different from those extracted for CpI [30, 37].

With use of the light-induced ligand exchange procedure described above [34], two other CO ligands of the distal iron can be labeled with ^{13}C via exchange of the respective CO ligands during illumination of the H_{ox}–^{13}CO sample for 2–3 h at 273 K in the presence of ^{13}CO gas. This effect thus provides an opportunity to undertake a more detailed investigation of the distribution of the unpaired spin over the bridging CO and terminal CO ligands of the distal iron. The "scrambled" sample after illumination will be called H_{ox}–$(^{13}CO)_3$. The H_{ox}–$(^{13}CO)_3$ sample was probed by X-band HYSCORE using settings similar to those for the H_{ox}–^{13}CO sample to provide a direct comparison of the spectra.

As shown in Fig. 6, two additional sets of crosspeaks can be clearly identified in the HYSCORE spectra of H_{ox}–$(^{13}CO)_3$. Both of them are absent in the respective spectra of the H_{ox}–^{13}CO and the nonenriched samples.

One pair of peaks remains in the (++) quadrant in all HYSCORE spectra, which is an indication of a weak ($|2v_n| > |A|$) and rather isotropic hyperfine coupling. Another set of signals shows up in the (+−) quadrant at higher magnetic field (g_2), while at low field it is in the (++) quadrant, which shows the large anisotropy of this ^{13}C hyperfine coupling. The simulation of these HYSCORE spectra is also shown in Fig. 6; the parameters are listed in Table 2.

According to a recent FTIR study [31], the bridging CO ligand (CO_{br}) and the terminal CO ligand of the distal iron (CO_d) are exchanged with $^{13}CO_{ext}$ and free ^{13}CO upon illumination and thus become ^{13}C-labeled with an average efficiency of about 60% after 4 h. It has also been shown that the "scrambling" does not affect the terminal CO ligand of the proximal iron (CO_p). On the basis of that observation, the additional ^{13}C signals (A_{2C} and A_{3C}) were assigned to the CO_{br} and the CO_d ligands, respectively (Structure 1).

There is no direct evidence for which of these two observed signals corresponds to which CO ligand; however, some assumptions based on the character of the hyperfine tensors can be made. Our recent investigation of the ^{57}Fe hyperfine couplings [30] shows that the spin density is somewhat delocalized between the irons in the binuclear subcluster, which is also supported by the relatively large ^{13}C hyperfine coupling of CO_{ext} (A_{1C}). Therefore, the ^{13}C nucleus of the CO_{br} ligand is expected to have a large hyperfine coupling with a rhombic character of the hyperfine tensor rather than an axial one. Hence, we are inclined to assign the A_{2C} hyperfine tensor to the bridging CO ligand. Consequently, the other hyperfine coupling (A_{3C}) is assigned to the terminal CO ligand of the distal iron. According to density functional theory (DFT) calculations, no direct spin density is expected at this CO ligand [62]; therefore, a rather weak ^{13}C hyperfine coupling is expected. This fits to the character of the observed A_{3C} hyperfine coupling.

Discussion

Spin density distribution

Recently we presented a study of the ^{57}Fe-enriched [FeFe] hydrogenase in the H_{ox} and H_{ox}–CO state using pulse EPR spectroscopy [30]. It was found that both irons carry some spin density. On the basis of the observed ^{57}Fe hyperfine couplings it was suggested that most of the spin density is located around the proximal iron in the case of the H_{ox}–CO state, while for the H_{ox} state a complete delocalization over the two irons in the binuclear subcluster was proposed.
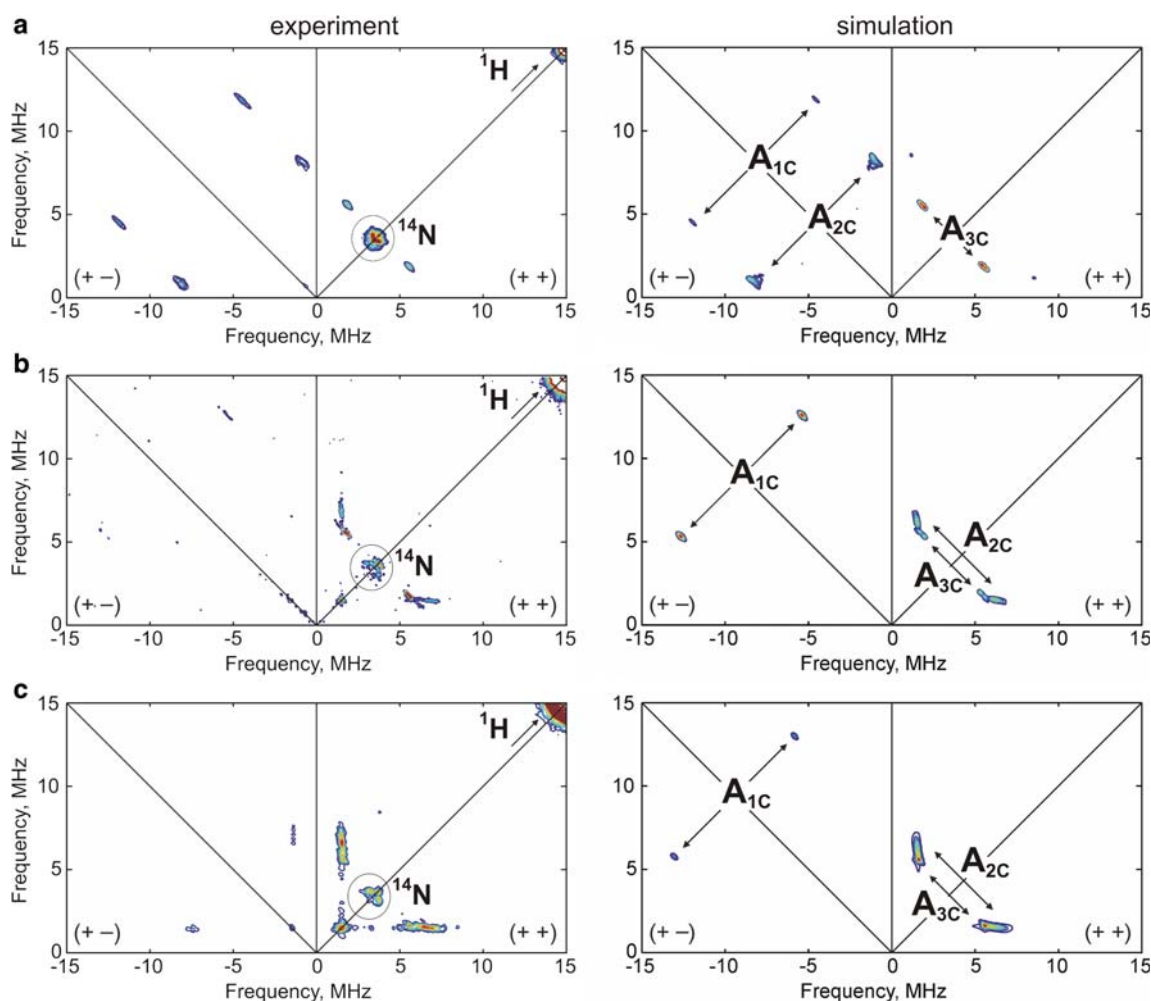
Fig. 6 X-band HYSCORE spectra of the H_{ox}–$(^{13}CO)_3$ state measured at several field positions (*left*) and corresponding simulations (*right*) accounting for three interacting ^{13}C nuclei using the parameters given in Table 2. The experimental conditions were as follows: t_1 and t_2 step 16 ns; shot repetition time 2 ms; B_0 **a** 346.2 mT (g_2), **b** 341.5 mT, **c** 337.0 mT (g_1); ν_{mw} **a** 9.7328 GHz, **b** 9.7469 GHz, **c** 9.7576 GHz; τ **a** 136 ns, **b, c** 120 ns

The relatively large ^{13}C hyperfine coupling found for the $^{13}CO_{ext}$ ligand of the distal iron may indicate that the spin delocalization is larger in the H_{ox}–CO state than was estimated from the ^{57}Fe hyperfine couplings.

According to recent theoretical calculations by Fiedler and Brunold [62], the unpaired spin in the H_{ox} state is located mostly at the distal iron, while in the case of the H_{ox}–CO state the spin density is distributed between both iron centers. When a complete H-cluster was taken into account, including all six iron atoms, the calculated Mulliken spin population ratio was found to be about 2:1 in favor of the proximal iron. For investigation of the electronic structure, Fiedler and Brunold used a truncated model [62] which consisted of only the binuclear subcluster. On the basis of the composition of the singly occupied molecular orbital it was observed that in this model spin density is more localized on the proximal iron (with a ratio of about 3.7:1 in favor of the proximal iron).

This shows that the "cubane" plays an important role in the electronic structure of the H-cluster. Unfortunately no calculations of EPR parameters have been presented for the complete 6Fe model. Some of the calculated values for the 2Fe models with protonated (ox^{SH}–CO) and not protonated (ox^S–CO) sulfur of the bridging Cys residue are compared with experimental data in Table 3.

In both calculated 2Fe models of the H_{ox}–CO state, the spin density around the distal iron is located in a d_{z^2}-shaped orbital and points towards the extrinsic CO ligand. An axial character of the extracted ^{13}C hyperfine coupling (A_{1C} in Table 2) supports this. Therefore, it is expected to find a strong coupling of the ^{13}C atom of CO_{ext} even if the ^{57}Fe hyperfine coupling on the distal iron is quite small. In general, this agrees with the experimental findings. Nevertheless, the closest calculated hyperfine coupling of 29 MHz (ox^{SH}–CO model in Table 3) is much larger than the one observed experimentally

Table 3 Comparison of the experimental and calculated isotropic ^{13}C hyperfine values and singly occupied molecular orbital (*SOMO*) composition ratio between Fe_p and Fe_d

	Experiment	DFT[a]	
		ox^{SH}–CO	ox^S–CO
^{13}C A_{iso}(CO$_{ext}$) (MHz)	17.1	29	53
SOMO (Fe$_p$:Fe$_d$)	5:1[b]	3.7:1	1.2:1

DFT density functional theory

[a] Values are adapted from [62]

[b] Ratio is estimated on the basis of the experimental data (see the text)

[A_{iso} (A_{1C}) = 17.1 MHz; Table 2]. Therefore, we conclude that the calculated spin population on the distal iron is overestimated.

In a first estimation we assume that the ^{13}C hyperfine coupling of the extrinsic CO ligand is proportional to the amount of spin density on the distal iron. Thus, to lower the ^{13}C hyperfine coupling to about 17 MHz, the spin population on the distal iron must be reduced about 2 times from what has been calculated. To achieve this, the spin density must be "shifted" towards the proximal iron. Consequently, the spin-population ratio between the proximal and the distal irons in the binuclear subcluster should be about 5:1 for the H$_{ox}$–CO state, which better agrees with the picture of a rather localized spin density, concluded from the analysis of the ^{57}Fe hyperfine interactions [30]. Therefore, despite the seemingly large ^{13}C coupling of CO$_{ext}$, we incline to the conclusion that the proximal iron carries most of the spin density in the H$_{ox}$–CO state.

In the H$_{ox}$ state we found an equal distribution of the unpaired spin density over both irons, on the basis of the ^{57}Fe hyperfine couplings [30]. This differs dramatically from the results of the DFT calculations [62] in which about 80% of the spin density was calculated to be localized at the distal iron. However, if we again assume that the spin population on the distal iron is overestimated 2–3 times, it would lead to the conclusion of an almost equal distribution of the unpaired spin density over both irons in the binuclear subcluster. This would fit the experimental data quite well.

One of the possible origins of this overestimation of the spin distribution on the distal iron by DFT may be the truncation of the H-cluster to a 2Fe model used for calculation of the spin distribution and EPR parameters. Nevertheless, only large-scale theoretical calculations of the structure and the magnetic resonance parameters could clarify this point. Moreover, we believe that the protein environment should also be taken appropriately into account to reproduce the experimental data.

Scrambling

Upon illumination of the H$_{ox}$–^{13}CO state, two other CO ligands of the distal iron can be exchanged with ^{13}CO [so-called H$_{ox}$–(^{13}CO)$_3$ state] [31, 34]. This result from FTIR spectroscopy has been corroborated by our EPR experiments. However, an exchange of the terminal CO ligand of the proximal iron was not completely excluded by the FTIR data.

According to our interpretation of the EPR data, the unpaired spin density is located at the proximal iron in H$_{ox}$–CO; therefore, it is expected, that the ^{13}CO ligand of this iron atom should produce sufficiently large ^{13}C hyperfine coupling (although it could be mostly dipolar), which should be detectable by either HYSCORE or ENDOR spectroscopy. However, neither of these methods showed any trace of a fourth ^{13}C hyperfine coupling, although a weakly coupled ^{14}N nucleus has been observed. Therefore, our results are in agreement with the notion that under the experimental conditions used only the CO ligands of the distal iron exchange upon illumination with sufficient rates.

Comparison with previous results

Our investigation has shown a quite anisotropic ^{13}C hyperfine coupling centered at $A_{iso} = 17.1$ MHz for the CO$_{ext}$ ligand (at Fe$_d$). The ENDOR study of Telser et al. [37] on the active site of CpI yielded a somewhat larger and more isotropic ^{13}C hyperfine coupling of $A_{iso} = 21.5$ MHz for the extrinsic CO ligand. The difference cannot be explained by the uncertainty of the experiment. As discussed in our previous paper [30], the ^{57}Fe hyperfine couplings are also different for these two species (DdH and CpI). We have observed that in the case of DdH both ^{57}Fe and ^{13}C hyperfine couplings are smaller than those found for the H-cluster in CpI. Therefore, it was concluded that the H-clusters of these two organisms are somewhat different in geometry, causing variations in the electronic structures. Unfortunately, no study on the H$_{ox}$–(^{13}CO)$_3$ state has been performed so far for CpI.

One possible origin of the difference in the electronic structure between the two species can be a difference in the exchange coupling between the [2Fe]$_H$ and the [4Fe–4S]$_H$ subcluster [29]. The formally diamagnetic [4Fe–4S]$^{2+}$ subcluster reveals strong ^{57}Fe hyperfine couplings due to an exchange interaction between the electronic spin of the closest iron of the "cubane" and the unpaired electron spin of the binuclear subcluster. As discussed by Popescu et al. [29], the exchange interaction between the [4Fe–4S]$_H$ and the [2Fe]$_H$ subcluster has a major influence on the detected spin distribution in these subunits. Apparently, this effect is not only observed in the hyperfine couplings of the ^{57}Fe

nuclei, but also in the general distribution of the unpaired spin.

Several attempts have been made to elucidate the influence of the $[4Fe–4S]_H$ subcluster on the electronic structure of the binuclear subcluster by quantum chemical methods [62, 63]. Schwab et al. [63] discovered that in the 6Fe model of the H-cluster a strong delocalization of the frontier molecular orbitals is observed. The electron density difference plot between the 6Fe cluster and separate 4Fe and 2Fe subclusters shows large changes in the molecular orbitals. This indicates a strong influence of the connected [4Fe–4S] subcluster on the electronic structure of the binuclear subcluster. Therefore, differences in the geometry of the $[4Fe–4S]_H$ subcluster from species to species may affect the $[4Fe–4S]_H–[2Fe]_H$ exchange interaction. In turn, this can alter the unpaired-spin distribution in the binuclear subcluster. As is known from X-ray crystallography, the $[4Fe–4S]_H$ subcluster is coordinated by Cys ligands, i.e., it is tightly bound to the protein environment. A geometrical difference in this part of the protein in DdH and CpI may be the reason for a difference in the geometry of the $[4Fe–4S]_H$ subcluster and thus in the electronic structure. Additionally, the protein surroundings may also affect the structure of the binuclear subcluster via electrostatic, dipole, and hydrogen-bonding interactions, as recently discussed [24].

Summary and conclusions

An extensive investigation of the distribution of the unpaired spin density over the ligands of the binuclear subcluster was performed for the H_{ox}–CO state of the H-cluster of DdH.

The ^{13}CO-inhibited state of the H-cluster (H_{ox}–^{13}CO) was studied by pulse EPR methods. A single ^{13}C hyperfine coupling was observed and assigned to the external CO ligand. The extracted isotropic part of the hyperfine coupling agrees with the previously obtained hyperfine coupling for DdH obtained by Roseboom et al. [31, 34]. Use of advanced EPR methods allowed us to resolve all principal values of the ^{13}C hyperfine coupling for the external CO ligand.

This hyperfine coupling, however, is substantially different with respect to both the isotropic and the anisotropic part from the one previously reported for CpI by Telser et al. [37, 39]; therefore, these results indicate a difference between the electronic structures of the H-cluster of these species. This has also been concluded from the observed ^{57}Fe hyperfine couplings [30].

The reaction of the H_{ox}–^{13}CO state with light was investigated. As observed earlier by Roseboom [31, 34], illumination between 275 and 278 K resulted in scrambling of the CO ligands in the binuclear subcluster and thus in a ^{13}C labeling of the terminal CO ligand of the distal iron and of the bridging CO ligand. For the first time ^{13}C hyperfine couplings of these ligands have been extracted, which give insight into the extent of the spin density distribution over the $[2Fe]_H$ subcluster.

In addition, the unlabeled H-cluster in the H_{ox}–CO state was investigated. A single weakly coupled ^{14}N nucleus was observed. This shows that there is some spin density at one of the CN ligands, while the other one carries negligible spin density.

These data allow a refinement of the spin-distribution picture of the H_{ox}–CO state. On the basis of the extracted hyperfine couplings we have concluded that although most of the spin density is indeed localized at the proximal iron, there is also a substantial distribution of the spin density over the distal iron and its CO ligands, but not over the CN ligands. On the basis of our results we conclude that the spin population at the proximal iron must be about 5 times larger than that at the distal iron in order for it to fit the experimental findings.

To summarize, we have mapped the distribution of the unpaired spin in the binuclear subcluster in the H_{ox}–CO state for all CO and CN ligands except for the CO ligand of the proximal iron. We believe that the data obtained will be useful for further theoretical studies aiming at a correlation of the electronic structure of the H-cluster and the function of the enzyme.

References

1. Cammack R, Frey M, Robson R (2001) Hydrogen as a fuel. Learning from nature. Taylor & Francis, London
2. Nath K, Das D (2004) Appl Microbiol Biotechnol 65:520–529
3. Kotay SM, Das D (2008) Int J Hydrogen Energy 33:258–263
4. Adams MWW (1990) Biochim Biophys Acta 1020:115–145
5. Vignais PM, Billoud B, Meyer J (2001) FEMS Microbiol Rev 25:455–501
6. Lubitz W, Reijerse EJ, van Gastel M (2007) Chem Rev 107:4331–4365
7. Lubitz W, van Gastel M, Gärtner W (2007) Met Ions Life Sci 2:279–322

8. Volbeda A, Charon M-H, Hatchikian EC, Frey M, Fontecilla-Camps JC (1995) Nature 373:580–587
9. Ogata H, Hirota S, Nakahara A, Komori H, Shibata N, Kato T, Kano K, Higuchi Y (2005) Structure 13:1635–1642
10. Chen JS, Mortenson LE (1974) Biochim Biophys Acta 371:283–298
11. Nicolet Y, Cavazza C, Fontecilla-Camps JC (2002) J Inorg Biochem 91:1–8
12. Pilak O, Mamat B, Vogt S, Hagemeier CH, Thauer RK, Shima S, Vonrhein C, Warkentin E, Ermler U (2006) J Mol Biol 358:798–809
13. Shima S, Thauer RK (2007) Chem Rec 7:37–46
14. Shima S, Pilak O, Vogt S, Schick M, Stagni MS, Meyer-Klaucke W, Warkentin E, Thauer RK, Ermler U (2008) Science 321:572–575
15. Lyon EJ, Shima S, Boecher R, Thauer RK, Grevels FW, Bill E, Roseboom W, Albracht SPJ (2004) J Am Chem Soc 126:14239–14248
16. Hatchikian EC, Magro V, Forget N, Nicolet Y, Fontecilla-Camps JC (1999) J Bacteriol 181:2947–2952
17. Peters JW, Lanzilotta WN, Lemon BJ, Seefeldt LC (1999) J Inorg Biochem 74:44
18. Peters JW, Lanzilotta WN, Lemon BJ, Seefeldt LC (1998) Science 282:1853–1858
19. Pierik AJ, Hulstein M, Hagen WR, Albracht SPJ (1998) Eur J Biochem 258:572–578
20. Nicolet Y, de Lacey AL, Vernede X, Fernandez VM, Hatchikian EC, Fontecilla-Camps JC (2001) J Am Chem Soc 123:1596–1601
21. Armstrong FA (2004) Curr Opin Chem Biol 8:133–140
22. Cao ZX, Hall MB (2001) J Am Chem Soc 123:3734–3742
23. Nicolet Y, Piras C, Legrand P, Hatchikian CE, Fontecilla-Camps JC (1999) Struct Fold Des 7:13–23
24. Pandey AS, Harris TV, Giles LJ, Peters JW, Szilagyi RK (2008) J Am Chem Soc 130:4533–4540
25. Patil DS, Moura JJG, He SH, Teixeira M, Prickril BC, Dervartanian DV, Peck HD, Legall J, Huynh BH (1988) J Biol Chem 263:18732–18738
26. Pereira AS, Tavares P, Moura I, Moura JJG, Huynh BH (2001) J Am Chem Soc 123:2771–2782
27. Pierik AJ, Hagen WR, Dunham WR, Sands RH (1992) Eur J Biochem 206:705–719
28. Nicolet Y, Lemon BJ, Fontecilla-Camps JC, Peters JW (2000) Trends Biochem Sci 25:138–143
29. Popescu CV, Münck E (1999) J Am Chem Soc 121:7877–7884
30. Silakov A, Reijerse EJ, Albracht SPJ, Hatchikian EC, Lubitz W (2007) J Am Chem Soc 129:11447–11458
31. Roseboom W, de Lacey AL, Fernandez VM, Hatchikian C, Albracht SPJ (2006) J Biol Inorg Chem 11:102–118
32. Lemon BJ, Peters JW (1999) Biochemistry 38:12969–12973
33. Lemon BJ, Peters JW (2000) J Am Chem Soc 122:3793–3794
34. Albracht SPJ, Roseboom W, Hatchikian C (2006) J Biol Inorg Chem 11:88–101
35. Patil DS, He SH, Dervartanian DV, Legall J, Huynh BH, Peck HD (1988) FEBS Lett 228:85–88
36. Chen ZJ, Lemon BJ, Huang S, Swartz DJ, Peters JW, Bagley KA (2002) Biochemistry 41:2036–2043
37. Telser J, Benecky MJ, Adams MWW, Mortenson LE, Hoffman BM (1986) J Biol Chem 261:3536–3541
38. Telser J, Benecky MJ, Adams MWW, Mortenson LE, Hoffman BM (1987) J Biol Chem 262:6589–6594
39. Telser J, Benton PMC, Peters JW, Hoffman BM (2005) Advanced paramagnetic resonance studies of the Fe-only hydrogenase I from Clostridium pasteurianum (CpI), Conference Abstracts of ICBIC-12
40. Kamp C, Silakov A, Winkler M, Reijerse E, Lubitz W, Happe T (2008) BBA Bioenergetics 1777:410–416
41. Sienkiewicz A, Smith BG, Veselov A, Scholes CP (1996) Rev Sci Instrum 67:2134–2138
42. Epel B, Gromov I, Stoll S, Schweiger A, Goldfarb D (2005) Concepts Magn Reson B Magn Reson Eng 26B:36–45
43. Hyde JS, Pasenkiewicz-Gierula W, Jesmanowicz A, Antholine WE (1990) Appl Magn Reson 1:483–496
44. Höfer P, Grupp A, Nebenfuhr H, Mehring M (1986) Chem Phys Lett 132:279–282
45. Schweiger A, Jeschke G (2001) Principles of pulse electron paramagnetic resonance. Oxford University Press, New York
46. Rowan LG, Hahn EL, Mims WB (1965) Phys Rev 137:A61
47. Gemperle C, Aebli G, Schweiger A, Ernst RR (1990) J Magn Reson 88:241–256
48. Davis JL, Mims WB (1978) Rev Sci Instrum 49:1095–1097
49. Stoll S (2005) J Magn Reson 177:390–403
50. The Mathworks (2002) MATLAB 6.5. The MathWorks, Natick
51. Shane JJ, Hofer P, Reijerse EJ, de Boer E (1992) J Magn Reson 99:596–604
52. Tyryshkin AM, Dikanov SA, Goldfarb D (1993) J Magn Reson A 105:271–283
53. Hatchikian EC, Forget N, Fernandez VM, Williams R, Cammack R (1992) Eur J Biochem 209:357–365
54. van der Westen HM, Mayhew SG, Veeger C (1978) FEBS Lett 86:122–126
55. Hagen WR, Vanberkelarts A, Krusewolters KM, Dunham WR, Veeger C (1986) FEBS Lett 201:158–162
56. Cline JF, Janick PA, Siegel LM, Hoffman BM (1985) Biochemistry 24:7942–7947
57. Moriaud F, Gambarelli S, Lamotte B, Mouesca JM (2001) J Phys Chem B 105:9631–9642
58. Lucken EAC (1969) Nuclear quadrupole coupling constants. Academic Press, London
59. Willems JP, Reijerse EJ, Deboer E (1994) Mol Phys 83:1155–1169
60. Fan HJ, Hall MB (2001) J Am Chem Soc 123:3828–3829
61. Dikanov SA, Tyryshkin AM, Bowman MK (2000) J Magn Reson 144:228–242
62. Fiedler AT, Brunold TC (2005) Inorg Chem 44:9322–9334
63. Schwab DE, Tard C, Brecht E, Peters JW, Pickett CJ, Szilagyi RK (2006) Chem Commun 35:3693–3698